Plasma Sources Science and Technology

An investigation of CO_2 splitting using nanosecond pulsed corona discharge: effect of argon addition on CO_2 conversion and energy efficiency

To cite this article: M S Moss *et al* 2017 *Plasma Sources Sci. Technol.* **26** 035009

OPEN ACCESS
IOP Publishing
Plasma Sources Science and Technology
Plasma Sources Sci. Technol. **26** (2017) 035009 (18pp)
https://doi.org/10.1088/1361-6595/aa5b1d

An investigation of CO_2 splitting using nanosecond pulsed corona discharge: effect of argon addition on CO_2 conversion and energy efficiency

M S Moss[1], **K Yanallah**[1], **R W K Allen**[1] **and F Pontiga**[2]

[1] Department of Chemical and Biological Engineering, University of Sheffield, United Kingdom
[2] Departamento de Física Aplicada II, Universidad de Sevilla, Spain

E-mail: MMoss1@sheffield.ac.uk

Received 20 June 2016, revised 20 December 2016
Accepted for publication 20 January 2017
Published 22 February 2017

Abstract

The plasma chemical splitting of carbon dioxide (CO_2) to produce carbon monoxide (CO) in a pulsed corona discharge was investigated from both an experimental and a numerical standpoint. High voltage nanosecond pulses were applied to a stream of pure CO_2 and its mixture with argon, and the gaseous products were identified using Fourier transform infrared spectroscopy. Due to the shape of pulses, the process of CO_2 splitting was found to proceed in two phases. The first phase is dominated by ionization, which generates a high electron density. Then, during the second phase, direct electron impact dissociation of CO_2 contributes to a large portion of CO production. Conversion and energy efficiency were calculated for the tested conditions. The conversions achieved are comparable to those obtained using other high pressure non-thermal discharges, such as dielectric barrier discharge. However, the energy efficiencies were considerably higher, which are favorable to industrial applications that require atmospheric conditions and elevated gas flow rates.

Keywords: CO_2 splitting, corona discharge, nanosecond pulses

(Some figures may appear in colour only in the online journal)

1. Introduction

Carbon dioxide mitigation technologies are at the forefront of most governments' minds in order to limit the global temperature rise to 2 °C above pre-industrial levels [1]. In the recent past, carbon dioxide has been seen as an unwanted waste product with an associated cost and energy penalty to deal with. However, newer technologies are emerging which envision the ample quantity of CO_2 available from waste gas streams as a feedstock for the synthesis of green chemicals.

Unfortunately, CO_2 is a highly stable molecule and to achieve its thermal reduction to carbon monoxide requires temperatures in excess of 3000 K. Non-thermal plasmas can be beneficial to solve this problem since only the electron temperature in the gas is elevated. Furthermore, it is known that cumulative vibrational excitations of the CO_2 molecule can result in a highly energy efficient stepwise dissociation, as explained by Fridman [2]. Therefore, carbon dioxide splitting using non-thermal plasmas is nowadays being considered as a possible pathway to produce synthetic fuels via a CO intermediate. Many different approaches to non-thermal plasma splitting of CO_2 have been followed, but most research has been focused on dielectric barrier discharges (DBD), microwave plasmas and gliding arc discharges [2]. In this work, pulsed corona discharge using a wire-to-cylinder reactor will be considered. The design of the reactor is simple and it operates at atmospheric pressure, making it suitable for upscaling. Indeed, corona discharges have already demonstrated

0963-0252/17/035009+18$33.00

their applicability on an industrial level in electrostatic precipitators for particulate removal in waste gas streams.

The majority of past works on pulsed corona discharge have been focused on gas cleaning technologies for NO_x, SO_x, VOCs and H_2S removal. These studies have shown that a significant percentage of the undesired molecules can be destroyed with a high efficiency. For example, in the work of Yamamoto *et al* [3], wire-to-cylinder microsecond pulsed corona discharge was applied for toluene, methylene chloride and CFC-113 removal with excellent results. Helfritch [4] employed a similar approach for H_2S removal, again with a great efficiency. The use of pulsed corona to reduce NO_x and SO_2 emissions in flue gases from a coal thermal plant has also tested by Dinelli *et al* [5].

The application of corona discharge for the decomposition of CO_2 has been less investigated, and even less the utilization of pulsed corona discharge. This latter technique was applied by Malik *et al* [6] to decompose a mixture of CO_2 and methane (CH_4) (1:1 ratio) using a wire-to-cylinder reactor. They applied 4 μs width pulses with maximum amplitude of 45 kV, and they achieved decompositions of 38% for CO_2 and 46% for CH_4, at a flow rate of 10 cm^3 min^{-1}. However, under these conditions, the energy efficiency was low (2.5%). The authors also investigated the decomposition of pure CO_2 with some success, obtaining a maximum reduction of 16.8%. Similarly, Bak *et al* [7] applied nanosecond pulsed high voltage between the flat ends of two cylindrical electrodes separated by a short distance. The experiments were carried out in pure CO_2 under pressurized conditions (2.4 atm–5.1 atm) and they achieved the maximum conversion rate of CO_2 into CO at the highest tested pressure, with a value of 7.3%, while the best energy efficiency (11.5%) was obtained at the lowest pressure. The authors explained this result through the reduced electric field, being lower at higher pressures. Moreover, they performed an energy balance of reactions in the CO_2 plasma and concluded that the dominant dissociation pathway goes through electronic excitation of CO_2 (10.5 eV) followed by autodissociation into CO and O.

Using DC wire-plate corona discharge, Xu *et al* [8] reported a maximum CO_2 decomposition of 10.91% for a gas flow rate of 30 cm^3 min^{-1}, although the energy efficiency was, at most, about 6.73%. The authors concluded that higher flow rates and lower discharge powers increase the energy efficiency at the cost of a lower conversion. Similarly, Mikoviny *et al* [9] investigated CO_2 reduction in pure CO_2 and in its mixture with O_2 with a flow rate of 100 cm^3 min^{-1}. They used a wire-to-cylinder reactor operated at negative polarity, in the range 4.5–6.5 kV. The conversion of CO_2 to CO was very small, but they observed an increase of CO production by rising the percentage of oxygen in the gas mixture.

Horváth *et al* [10] also investigated the application of positive and negative DC corona to pure CO_2 using a wire-to-cylinder reactor, but they carried out the experiment in a static regime, that is, under stopped-flow conditions. Their results showed that negative DC corona yield a better conversion to CO (over 10% at 7.5 kV). The decomposition of CO_2 in mixtures with N_2 under flow-stopped conditions was studied by Pontiga *et al* [11]. They used negative wire-to-cylinder corona discharge, and they also simulated the problem using a chemical model of 37 chemical species. The amount of CO formed during the operation of the reactor was of the order of a few percent, while O_3 formation was in the range of fractions of one percent. The authors observed that the formation of NO_x inhibits the generation of O_3 and prevent the growth of CO over time. In a later work [12], they extended that investigation to positive corona using the same reactor. They found that in CO_2-rich gas mixtures (>90%), the corona discharge became unstable and extinguished after running the discharge for some time. Then, voltage needed to be increased to stabilize the discharge. Moreover, they found that the electrical discharge exhibited two current regimes, depending on the ratio CO_2:N_2. In gas mixtures with a high percentage of CO_2 (60%–80%), the corona current level was high and NO_x, and particularly NO, was readily produced. In contrast, for low percentages of CO_2 (20 to 40%), the corona current level was much lower, and O_3 and N_2O was easily detected.

Numerical modeling is of great importance to increase the understanding of processes which take place inside plasmas, and it constitutes a valuable tool to determine the fundamental mechanisms leading to CO_2 splitting. Models can also provide a description of quantities which are difficult, if not impossible, to measure in experiments, such as time and spatial dependence of reaction rates. However, deciding which reactions must be included in the numerical simulation is a difficult task. In early modeling of CO_2 lasers, where the laser medium usually consists of a flowing CO_2–N_2–He mixture, hundreds of reactions have been proposed to participate in the plasma chemistry [13, 14]. Therefore, the selection of reactions that are relevant to the target system is crucial to yield accurate predictions of experimental measurements. Of course, there is always a trade-off between accuracy and time efficiency in numerical simulations, since including more reactions and species increases the computational time.

One of the most comprehensive comparative studies between plasma modeling and experiments in CO_2 has been undertaken by the PLASMANT research group, mainly for DBD [15, 16]. They have carried out numerous 0D kinetic studies using the GlobalKin code of Kushner and co-workers, both for studying CO_2 reduction in pure CO_2 and its admixtures with argon/helium [17], and for dry-reforming of methane [18]. Particularly notable are their investigations of the role of vibrational states on CO_2 splitting [19, 20]. They concluded that this pathway constitutes the dominant mechanism for CO_2 dissociation in microwave discharges, while it is of secondary importance in DBD. Focusing on pure CO_2, their modeling gave excellent correlation with experimental results for specific energy inputs (SEI) below 100 J cm^{-3}. The maximum conversion achieved experimentally was 35%, with an energy efficiency of 2% [15]. However, energy efficiencies up to 8% were obtained at the expense of reducing CO_2

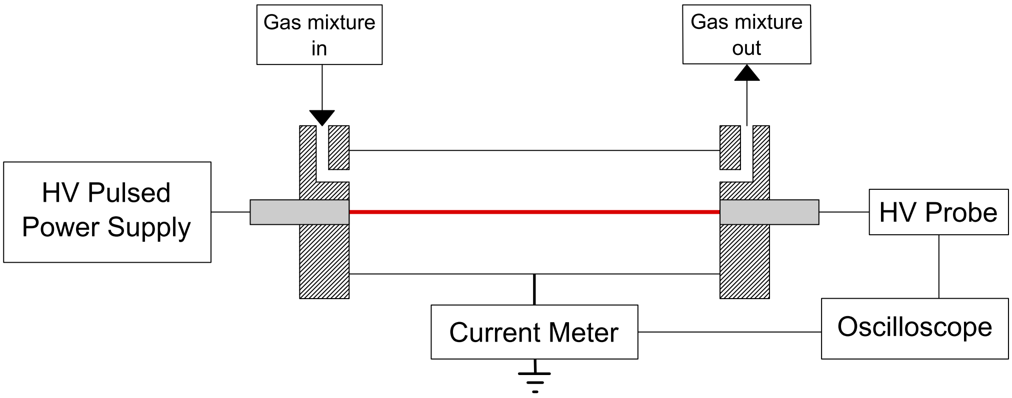

Figure 1. Schematic of experimental system.

conversion to a few percent. More recently, Snoeckx *et al* [21] have carried out numerical modeling and experiments in CO_2/N_2 mixtures. Their motivation was the DBD treatment of impure CO_2 streams, with N_2 as the main industrial impurity. They found that CO_2 conversion and energy efficiency increases more or less exponentially with rising N_2. In gas mixtures with a large nitrogen fraction (~90%), the reported CO_2 conversion was about 18%, with an energy efficiency of 20%, approximately. However, lowering the nitrogen content quickly reduces conversion and efficiency.

Regarding corona discharge, Yanallah *et al* [22, 23] have simulated positive and negative DC corona discharge in carbon dioxide for a wire-to-cylinder electrode configuration. In these studies, the experimental voltage and current were used as inputs for the numerical simulation. However, in the present work, only the experimental voltage is required. They computed the distribution of species using a 2D model, and compared their findings with the experimental concentrations of CO and O_3 for gas flow rates of 20 and 100 $cm^3\ min^{-1}$ and different applied voltages. The production of CO was below 1%, and the agreement between modeling and experiments was excellent.

In this work, an experimental and modeling study on CO_2 splitting using pulsed corona discharge is presented, both in pure CO_2 and its mixtures with Ar. The main aim of this research is twofold: (1) to maximize the conversion of CO_2 into CO and (2) to minimize the energy required to achieve this transformation. The experiments have been carried out for different gas flow rates and gas compositions, and the results are analyzed and compared with the predictions from the numerical simulation. The computational model is a combination of a one-dimensional and a zero-dimensional model, so that the complex plasma chemistry of CO_2 can be successfully dealt, including the vibrational levels of the CO_2 molecule. The 1D model treats a single pulsed discharge, and their results are used in the 0D model to simulate the plasma chemistry of corona discharge over long times. From the results of this combined technique, the mechanism of CO_2 splitting in a pulsed corona discharge can be hypothesized and compared to those of other non-thermal plasmas.

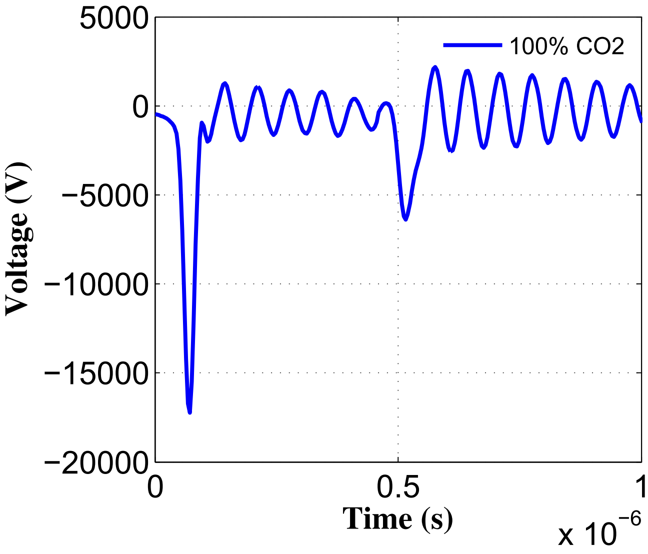

Figure 2. Oscillogram of the voltage applied to the reactor for pure CO_2.

2. Description of the work

2.1. Experimental setup

Figure 1 shows a schematic diagram of the experimental equipment. All experiments were carried out at atmospheric pressure and ambient temperature. The wire-to-cylinder corona discharge reactor was formed by a stainless steel cylinder as the outer electrode, with radius $R = 17$ mm, and a thin tungsten wire as the inner electrode, with radius $r_0 = 125\ \mu m$. The length of the reactor was 30 cm.

A high voltage pulse generator (NPG18-3500N Megaimpulse Ltd [24]) was used to energize the inner wire. The connection between the pulse generator and the corona wire was made by means of a 75 Ω coaxial cable. The voltage signal applied to the wire was measured using a high voltage probe (Tektronix P6015A) connected to the live electrode. Regarding the corona current, a wide band current transformer (Pearson 6595) was used. The current transformer was fitted around the cable that connects the cylinder to ground. The voltage signals from both the high voltage probe and the current transformer

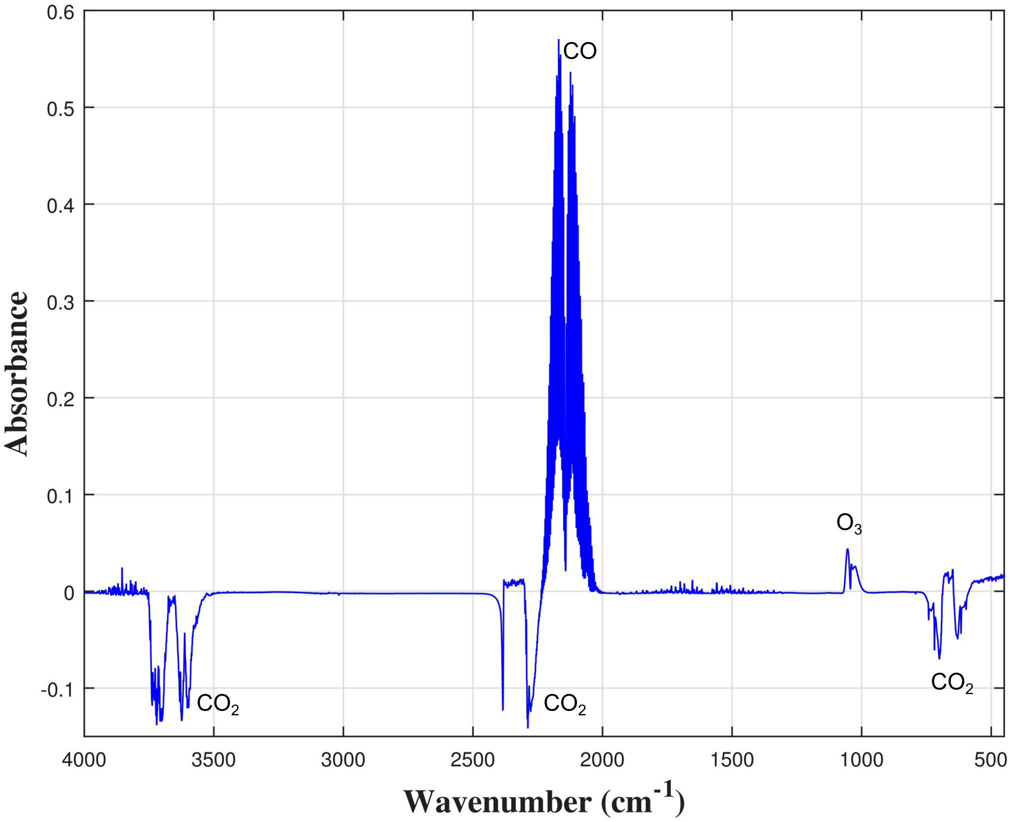

Figure 3. Sample spectrum after background correction showing the presence of CO in the exhausting gas.

were recorded in a high resolution oscilloscope (6404c Picotech). In order to minimize the time delay between the two signals, coaxial cables of similar lengths were used for the high voltage probe and the current transformer. A typical oscillogram of the voltage signal applied to the reactor, as measured with the high voltage probe, is shown in figure 2. It consists of a train of pulses, in which a first pulse, of high amplitude and short rise time, is followed by a series of pulses of smaller amplitude. Hereinafter, the term 'pulse' will be used to denote the entire voltage signal, while the term 'sub-pulse' will be used to refer to each distinct pulse within the voltage signal. The characteristic width of sub-pulses is about 40 ns and the total duration of a complete pulse is of about one microsecond. The short duration of pulses remove the need for a dielectric layer, prevent gas heating (thus increasing the efficiency of CO_2 splitting) and reduce the possibility of plasma arc development. The repetition frequency of pulses could be adjusted in the range 50–1700 Hz. As shown in figure 2, the applied peak voltage across the electrodes had a potential up to 17 kV. However, the amplitude and the voltage waveform are strongly affected by the impedance matching between the reactor and the power supply.

During experiments, a mixture of pure CO_2 (99.999%) and Ar (99.9%) was fed into the reactor in the axial direction. A mixing chamber was installed before the reactor entrance, in order to ensure a homogeneous gas mixing. The gas flow rates were controlled by means of mass flow controllers (Bronkhorst), and the total gas flow rate was varied in the range 100–800 $cm^3 min^{-1}$. After passing through the discharge reactor, gaseous products were analyzed by means of a Fourier transform infrared spectrometer (FTIR) (Varian 660-IR Agilent) *ex situ*. A typical spectrum, corrected with the background of the initial gas mixture, is shown in figure 3. The positive values of absorbance in the wavelength range 2025–2225 cm^{-1} corresponds to the formation of CO. The presence of ozone is also observed around 1054 cm^{-1}. In contrast, the negative values of the absorbance indicate the decomposition of CO_2.

2.2. Computational model

Atmospheric pressure corona discharges can be modeled using the so-called fluid approximation, which consists in solving continuity equations for every species produced in the electrical discharge, coupled with Poisson's equation [25–27]. However, the numerical simulation of pulsed discharges of nanosecond duration is a complex task, since the set of differential equations becomes a stiff system. This is due to the formation of sharp gradients of the species densities and of the electric field during the development of pulses. Additionally, the time required to carry out the simulation can be very large, and it increases further upon adding complexity to the model through the inclusion of more chemical species.

The strategy adopted in this work has been to use a combination of two solvers: COMSOL Multiphysics [28] and ZDPlaskin [29]. The DC plasma module within COMSOL has been first used to simulate the electrical discharge in 1D for the duration of a single pulse. In this part, the continuity and Poisson's equations have been solved in conjunction with Boltzmann equation. As a result, the electron density and reaction rate constants that involve electrons (e.g. dissociation, excitation, ionization and elastic collisions with neutral molecules) have been evaluated. These magnitudes are then averaged over radial distance and transferred to ZDPlaskin, where the 0D modeling of multi-pulses will be carried out.

It must be emphasized that the reaction rate constants that are used in the 0D model are not obtained from the averaged electron energy or the averaged electric field, but by directly averaging the reaction rate constants already evaluated in 1D model. The first procedure would produce less accurate results, as would also occur if a simple estimation of the electric field were used to obtain the reaction rate constants, which is very frequent in 0D simulations [15]. Furthermore, the accuracy of the method followed in this paper has been tested by solving the 0D model in many different points along the radial direction. The species densities so obtained were then averaged over the radial coordinate and compared with those computed using the spatially averaged reaction rate constants. A satisfactory agreement was found between the two approaches.

The need for splitting the modeling in two parts is imposed by the long computational time that would otherwise be required if the simulation were entirely done using the 1D model. Therefore, efforts have directed towards simplifying the calculation procedure but maintaining the precision of the modeling. The approach adopted in the present work provides more insight into the development of pulses and a more detailed picture of the temporal evolution of species during the process of CO_2 splitting.

2.2.1. The 1D fluid model. As revealed through experiments [7, 30, 31], the transition from corona to spark discharge is accompanied by instabilities in the electric current and it is dependent on the applied voltage, frequency, wire surface state, reactor geometry and gas mixture. For example, increasing the percentage of Argon favors the development of a spark. In our experiments, the electrical discharge was operated within the corona regime, and it appeared as a homogeneous glow that filled the entire reactor volume. Therefore, the electrical discharge will be modeled as a homogeneous discharge along the axial and azimuthal directions. With these assumptions, the problem becomes one-dimensional and the computational domain extends from the wire surface up to the surrounding cylinder along the radial coordinate. The axial dependence can be disregarded owing to the short duration of the pulse ($\sim 1\ \mu$s) as compared to the residence time of the gas inside the reactor. The electrical discharge can then be successfully described by a set of continuity equations, one for each species taking part in the discharge, coupled to Gauss' law for the electric field and to the electron energy equation. In polar coordinates, these equations can be written as:

$$\frac{\partial N_i}{\partial t} + \frac{1}{r}\frac{\partial}{\partial r}\left[r\frac{e_i}{|e_0|}\mu_i N_i E - rD_i\frac{\partial N_i}{\partial r}\right] = S_i, \tag{1}$$

$$\frac{\partial N_j}{\partial t} - \frac{1}{r}\frac{\partial}{\partial r}\left[rD_j\frac{\partial N_j}{\partial r}\right] = S_j, \tag{2}$$

$$\begin{aligned}\frac{\partial N_\varepsilon}{\partial t} &+ \frac{1}{r}\frac{\partial}{\partial r}\left[-r\mu_\varepsilon N_\varepsilon E - rD_\varepsilon\frac{\partial N_\varepsilon}{\partial r}\right]\\ &+ E\left[-\mu_e N_e E - D_e\frac{\partial N_e}{\partial r}\right] = S_\varepsilon,\end{aligned} \tag{3}$$

$$\frac{1}{r}\frac{\mathrm{d}}{\mathrm{d}r}(rE) = \frac{1}{\varepsilon_0}\sum_i e_i N_i, \tag{4}$$

$$E = -\frac{\mathrm{d}\phi}{\mathrm{d}r}, \tag{5}$$

where subscripts i, j, e and ε refer, respectively, to the ith charged species (electrons included), to the jth neutral species, to electrons (specifically), and to the electron energy per unit of charge; N denote density, D is the diffusion coefficient, S represents the gain/loss term, μ is the mobility, e_i is the electrical charge of the ith charged species, e_0 is the elementary charge, E is the electric field, ϕ is the electric potential and ε_0 is the dielectric constant of the gas.

The gain/loss rate of the nth species (charged or neutral) takes the form

$$S_n = \sum_j k_j N_l N_m \ldots, \tag{6}$$

where N_l, N_m, … are the number densities of species that participate as reactants in the jth reaction, with reaction rate constant k_j. The summation extends over all reactions involving the nth species, but the contribution of losses has negative sign. Reactions and species selected for the 1D model are highlighted in boldface in table A1 (see appendix). More details about the species will be given in the next section (0D model).

Similarly, the gain/loss of electron energy density can be expressed as

$$S_\varepsilon = \sum_j k_j \Delta\varepsilon_j N_e N_m \ldots, \tag{7}$$

where N_e is the electron number density and $\Delta\varepsilon_j$ is the energy gain/loss in the jth reaction.

The relaxation of vibrational states may produce an augmentation of the gas temperature. However, as it will be shown in section 3.1, the accumulation of vibrational states in a pulsed corona discharge is relatively low. Therefore, in this model, the temperature of the gas is assumed to be constant and equal to the ambient temperature.

The Scharfetter–Gummel upwind scheme of COMSOL has been adopted to integrate the set of continuity equations. This scheme has been used previously by Boeuf [27], Kulikovsky [32] and other authors, and it has demonstrated to be stable and adequate for the simulation of electrical discharges.

Integration of (1) and (5) require appropriate boundary conditions. At both electrodes, charged carriers (electrons and ions) are lost due to random motion within a few mean free paths from the walls, and electrons are gained at the cathode through secondary electron emission. This last process consists in the generation of electrons due to the bombardment of the cathode by positive ions, and it is essential to sustain the discharge. The boundary conditions for the electron density and the electron energy density are implemented as follows,

$$\mathbf{\Gamma}_e \cdot \mathbf{n} = \tfrac{1}{2} v_{e,\mathrm{th}} N_e - \sum_p \gamma_p \mathbf{\Gamma}_p \cdot \mathbf{n}, \text{ at } r = r_0 \text{ and } r = R, \quad (8)$$

$$\mathbf{\Gamma}_\varepsilon \cdot \mathbf{n} = \tfrac{5}{6} v_{e,\mathrm{th}} N_\varepsilon - \sum_p \varepsilon \gamma_p \mathbf{\Gamma}_p \cdot \mathbf{n}, \text{ at } r = r_0 \text{ and } r = R, \quad (9)$$

where $\mathbf{n}$ is the normal unit vector pointing towards the wall, $\mathbf{\Gamma}_e = -\mu_e \mathbf{E} N_e - D_e \nabla N_e$ is the flux of electrons, $\mathbf{\Gamma}_\varepsilon = -\mu_\varepsilon \mathbf{E} N_\varepsilon - D_\varepsilon \nabla N_\varepsilon$ is the flux of electron energy, $\mathbf{\Gamma}_p = \mu_p \mathbf{E} N_p - D_p \nabla N_p$ is the flux of the pth positive ions, ε is the mean energy of secondary electrons, γ_p is the secondary emission coefficient, and $v_{e,\mathrm{th}}$ is the thermal velocity of electrons, which is a function of the electron energy and, therefore, of the electric field. Secondary electron emission is assumed to take place only at the wire when it is acting as the cathode, with a coefficient value of 0.01. Otherwise it is set $\gamma_p = 0$. At the cylinder, owing to its large curvature radius, secondary electron emission is ignored, even when its polarity is negative with respect to the wire.

Regarding positive and negative ions, their boundary conditions at the electrodes are expressed as

$$\mathbf{\Gamma}_i \cdot \mathbf{n} = \tfrac{1}{2} v_{i,\mathrm{th}} N_i, \text{ at } r = r_0 \text{ and } r = R, \quad (10)$$

where $\mathbf{\Gamma}_i = (e_i/e_0)\mu_i \mathbf{E} N_i - D_i \nabla N_i$ is the flux of the ith ion, and $v_{i,\mathrm{th}}$ its thermal velocity.

The electrodes may constitute a source of neutral particles due to the neutralization of ions (e.g., CO_2^+ is converted into CO_2 on the cathode). Therefore, a balance equation between the fluxes of the ith ion and the corresponding jth neutral species must be written at the electrode in such a case,

$$\mathbf{\Gamma}_j \cdot \mathbf{n} = -\mathbf{\Gamma}_i \cdot \mathbf{n}, \text{ at } r = r_0 \text{ or } r = R. \quad (11)$$

Otherwise a null flux of the neutral species is set at the wall

$$\mathbf{\Gamma}_j \cdot \mathbf{n} = 0, \text{ at } r = r_0 \text{ or } r = R. \quad (12)$$

Finally, for the electrical potential, boundary conditions are simply expressed as

$$\phi(r_0) = V(t), \quad (13)$$

$$\phi(R) = 0, \quad (14)$$

where $V(t)$ is the impulse voltage applied to the corona wire, which is taken from the experimental measurements (see figure 2).

As for the initial conditions, the number densities of the CO_2 and Ar in the gas mixture were calculated according to the ideal gas law at atmospheric pressure (760 Torr) and ambient temperature (298 K). The densities of the other heavy species depend on the past history of the electrical discharge, since they are built with the occurrence of every single past discharge. However, for the 1D modeling of the pulse, these initial densities will be taken here as zero. This approximation is used to avoid a direct coupling between the 1D and 0D models, and to reduce the computational time of the simulation. Moreover, since electrons are mainly produced by direct ionization of the background CO_2 and Ar in the gas mixture, this simplification should have a negligible influence on the computed values of the electron number density and the electron energy density. Of course, the effect of accumulation of species with each pulse will be considered in the 0D modeling. Regarding the initial electron density, a small distribution of seed of electrons (10^6 cm^{-3}) with a Gaussian profile is introduced near the wire electrode. This initial electron density has the purpose of triggering the electric corona discharge pulse.

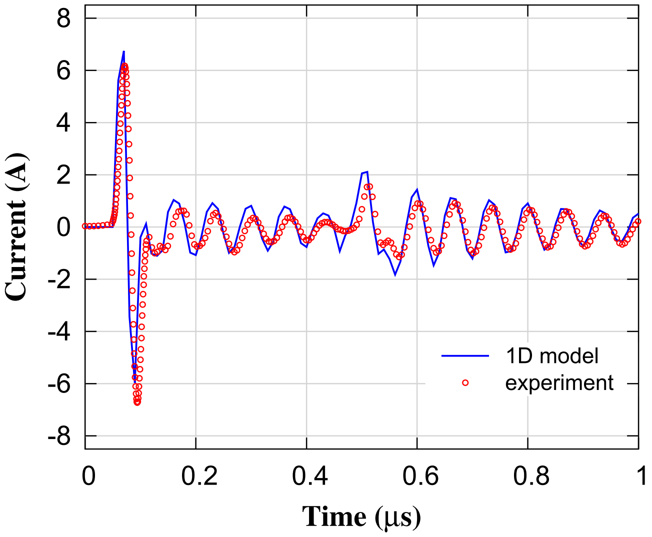

Figure 4. Temporal evolution of current intensity for the duration of a pulse in pure CO_2.

Figure 4 shows a comparison between the current intensity predicted by the 1D modeling and that measured during the experiments. Clearly, the agreement between simulation and experiment is quite satisfactory, which confirms that the hypotheses assumed in the 1D modeling are justified. Moreover, since the current intensity is linked to the drift of electrons and ions, this agreement also supports the correctness of the electron and energy densities predicted by the numerical simulation.

2.2.2. The 0D fluid model. After the completion of the 1D modeling, the electron density is passed to the 0D model, along with an accurate estimation of the reaction rate coefficients of reactions involving electrons. All plasma parameters are assumed to be spatially homogeneous in the 0D modeling. Therefore, the plasma reactor is considered as a batch reactor, which incorporates not only the reactions

Table 1. Species included in the 0D model.

Neutrals and radicals	Ar, CO_2, CO, C_2O, C, O_3, O_2, O
Positive ions	Ar^+, CO_2^+, CO^+, O_2^+, O^+
Negative ions	CO_3^-, CO_4^-, O_2^-, O^-
Excited species	Ar^*, $CO_2(v1)$, $CO_2(v2)$, $CO_2(v3)$, $CO_2(v4)$

already used in the 1D model, but also the rest of relevant reactions, i.e., ion–ion, molecule–ion and molecul–molecule reactions. The reaction rate constants of these additional reactions have been adopted from the literature and their values are listed in the appendix (see tables A2, A3 and A4).

The temporal evolution of the number densities of plasma species generated by the pulsed corona discharge is obtained from the resolution of the following set of coupled ordinary differential equations,

$$\frac{\partial N_j}{\partial t} = S_j \tag{15}$$

where integration is executed from $t = 0$ up to the residence time of the gas within the reactor. For this purpose, the ZDPlasKin code developed by Pancheshnyi *et al* [29] has been used.

The list of species considered in the 0D model is shown in table 1, and it includes, besides electrons, 8 neutral species, 5 positive ions, 4 negative ions and 5 excited species. The choice for these species was made after numerous tests, so as to select the species deemed to be most relevant to CO_2 splitting, both with and without the presence of Ar.

Following the approach of Aerts et *al* [19], the vibrational levels of CO_2 have been grouped in four effective levels (see table 2) in order to limit the number of species and chemical reactions. These levels are denoted as $CO_2(v1)$, $CO_2(v2)$, $CO_2(v3)$ and $CO_2(v4)$. $CO_2(v1)$ represents the first bending mode (010), $CO_2(v2)$ is the sum of the first symmetric stretch (100) and the second bending mode (020), and $CO_2(v3)$ is the first asymmetric stretch mode (001). Finally, the level $CO_2(v4)$ represents the sum of higher bending modes, like (030) and (040), with other modes of similar energies, like (110) and (120), respectively. Also, the contribution of other higher energy modes is gathered within $CO_2(v4)$. Vibrational states of CO and O_2 were neglected in this model, since their contribution to CO_2 splitting is minimal. Regarding excited electronic states of CO_2, they were only taken into account in the 1D modeling. As set out in Morgan's database [33] for electron collisions with argon, the excited electronic states of argon have been also grouped in a single species, Ar^*. It has been assumed that the excited states of a given species exhibit the same chemistry as its ground state, except for the energy threshold of reactions, which will be lower in the case of excited species.

Since the plasma kinetics of CO_2 is complicated and the aim of this work is on CO_2 splitting, the reaction scheme for Ar has been reduced to only five major processes (elastic, excitation, ionization, penning ionization of the excited states, and quenching of the excited states back to ground state).

Table 2. Notation of vibrational states used in the model and their effective energy level.

Species notation	States	Energy (eV)
CO_2	(000)	0
$CO_2(v1)$	(010)	0.083
$CO_2(v2)$	(020) + (100)	0.167
$CO_2(v3)$	(001)	0.291
$CO_2(v4)$	(030) + (110), (040) + (120), …	>0.25

3. Results and discussion

The energy efficiency and the conversion factor are the two most important parameters to be calculated in CO_2 splitting studies, and they are used extensively to compare different types of discharges. The absolute CO_2 conversion is defined as the change in CO_2 concentration over the initial CO_2 concentration. This can be assumed to approximately equal to the conversion to CO (or CO yield) since the production of other carbon containing products is negligible.

$$X_{\text{conv}}(\%) = \frac{[CO_2]_{\text{in}} - [CO_2]_{\text{out}}}{[CO_2]_{\text{in}}} \times 100 \approx \frac{[CO]_{\text{out}}}{[CO_2]_{\text{in}}} \times 100. \tag{16}$$

The effective conversion of CO_2 is defined as the product of the absolute conversion and the relative content of CO_2 in the CO_2/Ar gas mixture,

$$X_{\text{eff}}(\%) = X_{\text{conv}} \frac{[CO_2]_{\text{in}}}{[CO_2]_{\text{in}} + [Ar]} \times 100 \approx \frac{[CO]_{\text{out}}}{[CO_2]_{\text{in}} + [Ar]} \times 100. \tag{17}$$

The absolute energy efficiency η expresses the ratio of the dissociation enthalpy of CO_2,

$$CO_2 \rightarrow CO + \frac{1}{2}O_2, \quad \Delta H_R = 2.9 \text{ eV molecule}^{-1} = 283 \text{ kJ mol}^{-1} \tag{18}$$

to the actual energy cost, E_{CO}, to produce a single CO molecule in the reactor. Therefore, it can be written as

$$\eta(\%) = \frac{\Delta H_R}{E_{CO}} \times 100. \tag{19}$$

The value of E_{CO} can be obtained as the ratio of the energy E injected into the reactor during the residence time of the gas to the number of CO molecules, N_{CO}, that have left the reactor during the same interval of time, that is, $E_{CO} = E/N_{CO}$. The energy injected into the reactor can be evaluated as

$$E = f\, t_g E_{\text{pulse}} = f\, t_g \int_0^{\tau} V(t)\, I(t)\, dt, \tag{20}$$

where f is the frequency of pulses, t_g the residence time of the gas and E_{pulse} the energy delivered by a single pulse, which is equal to the integral over the duration of the pulse, τ, of the

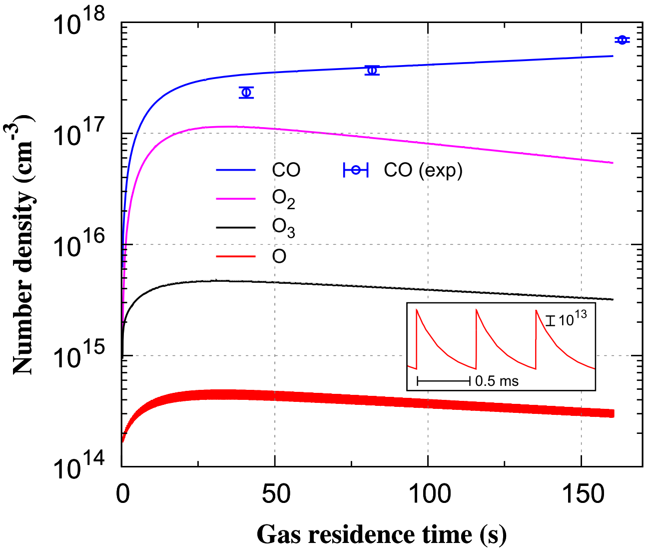

Figure 5. Number densities of the most important species generated by the nanosecond pulsed corona discharge in pure CO_2 as a function of residence time. Solid lines: numerical simulation. Dots: experimental measurements. The inset shows a magnification of O density (linear scale) around $t_g \approx 100$ s.

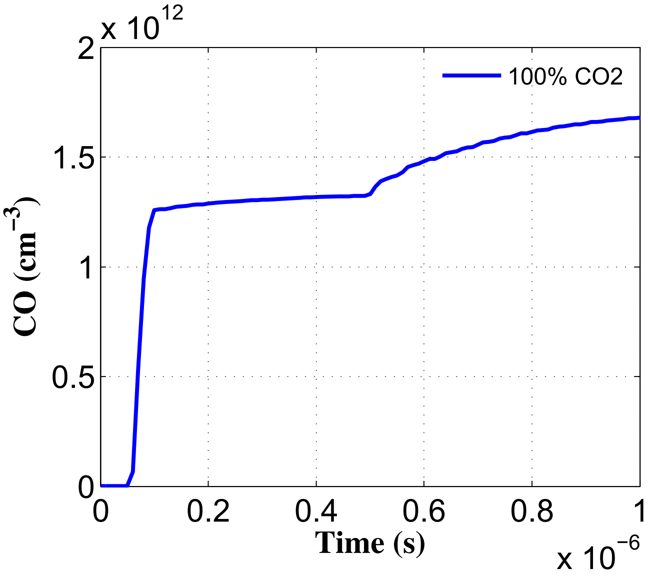

Figure 6. Temporal evolution of the spatially averaged CO density calculated from the 1D model during a single pulse (numerical simulation).

applied voltage $V(t)$ times the current intensity $I(t)$. Taking into account (16), the number of CO molecules that have exited the reactor during t_g is given by

$$N_{\mathrm{CO}} = X_{\mathrm{conv}}\,[\mathrm{CO_2}]_{\mathrm{in}}\,Q\ \ t_g, \tag{21}$$

where Q is the gas flow rate.

Equation (19) can be found in the literature in slightly different forms, particularly in terms of the SEI, which is defined as the ratio of the discharge power, $W = E/t_g$, to the gas flow rate Q, that is, $\mathrm{SEI} = W/Q$. Using the SEI, the energy cost can be expressed as $E_{\mathrm{CO}} = \mathrm{SEI}/(X_{\mathrm{conv}}[\mathrm{CO_2}]_{\mathrm{in}})$.

As it will be discussed later, the shape of the voltage waveform will have an important influence on the chemical kinetic pathway of CO_2 dissociation. The repetition frequency of pulses was fixed at 1.7 kHz, since higher frequencies introduces instabilities in the plasma discharge, thus reducing its homogeneity and increasing the gas temperature above 300 K. Under our experimental conditions, the reactor remained at nearly room temperature, and the energy deposited in the gas by the electrical discharge was changed by modifying the residence time of the gas, which is inversely proportional to the volumetric flowrate. The energy of a single pulse (as the one shown in figure 2) was estimated to be in the range of 1–2 mJ, depending on the gas mixture.

In the next section, the numerical and experimental results of pulsed corona in pure CO_2 will be first presented. Then, the effect of the addition of Ar and, particularly, its effect on the conversion factor and energy efficiency will be considered.

3.1. Results for pure CO_2

Figure 5 shows the behavior of neutral species in a pure CO_2 plasma as a function of the gas residence time. Besides carbon monoxide (CO), molecular oxygen (O_2), ozone (O_3) and atomic oxygen (O) are the main products resulting from the decomposition of CO_2. The typical number densities of these last species are, respectively, one, two and three orders of magnitude lower than that of carbon monoxide. The experimental measurements of CO density at the exit of the corona reactor are also shown in this figure by means of dots. The observed agreement between simulation and experiments confirms that the proposed model is sufficiently realistic to analyze the underlying chemical pathways of CO_2 splitting in nanosecond pulsed corona discharge operating in the glow regime. Differences can be attributed to the necessary simplifications introduced during the modeling and the uncertainty surrounding the reaction rate constants used in the simulation.

The temporal evolution of CO, O, O_2 and O_3 and, in general, of all species, is characterized by two distinct temporal scales: a short one, corresponding to the duration of each single pulsed discharge ($\sim 1\,\mu$s), and longer one, corresponding to the interval between two pulses ($\sim f^{-1} = 588\,\mu$s). During each pulse, the reactions initiated by electrons play a predominant role, and the number densities of species undergo sudden variations. This fact can be clearly appreciated for atomic oxygen in the inset of figure 5, but it is also present for the other species although with different amplitude. In particular, the concentrations of atomic oxygen and ozone increase with the initiation of each discharge, the first one by the effect of electron impact dissociation of CO_2 (E1), and the second one by the subsequent recombination of O with O_2 (N1). Conversely, the concentration of molecular oxygen decreases due its dissociation by electron impact (E12), and the formation of ozone (N1). During the interval between two consecutive pulses, reactions between neutral

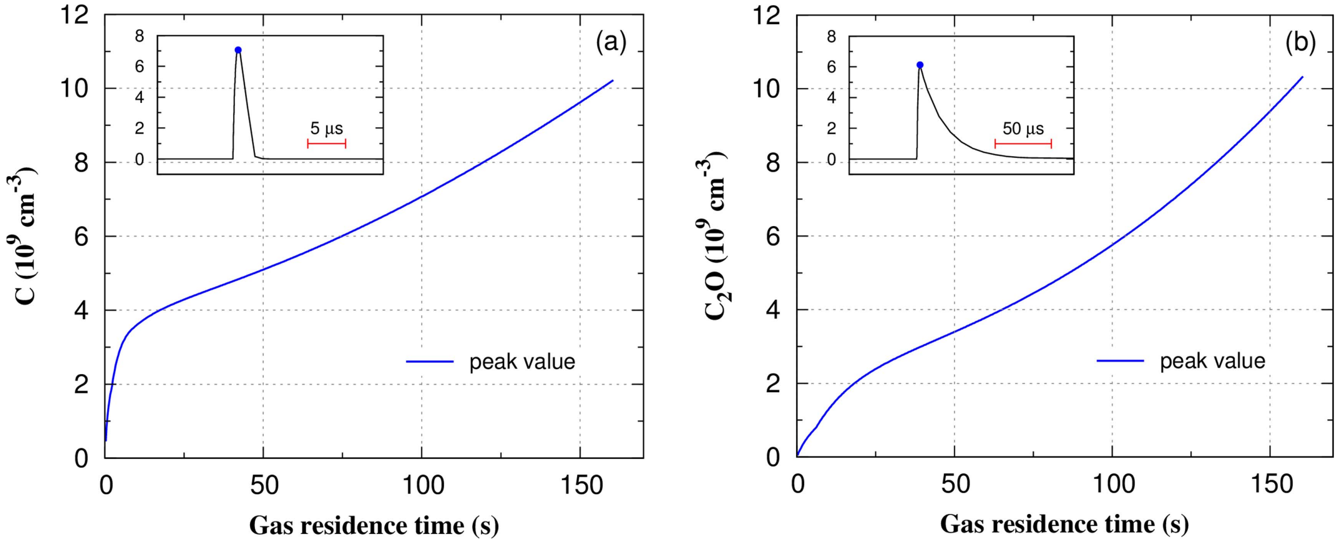

Figure 7. Peak values of the number densities of (a) C and (b) C_2O as a function of the gas residence time, t_g (numerical simulation). The insets show the temporal evolution of a single peak occurring at $t_g \approx 100$ s.

species still proceed, but the concentrations of species vary more slowly.

Over the long range temporal scale, the number densities of CO, O, O_2 and O_3 rise during the first 30 s, approximately. Then, the densities of O, O_2 and O_3 decline, due to their recombination with CO (reactions N5, N11, N12). In contrast, the growth rate of CO simply slows down after 30 s.

Figure 6 illustrates the splitting of CO_2 into CO for the duration of a single pulse. The CO density rises sharply during the first sub-pulse (~80 ns), which has an amplitude of approximately 17 kV. Subsequent sub-pulses, lower in magnitude, stabilize the formation of CO until 500 ns, where the second major sub-pulse contributes to another rise of CO density.

The contribution of individual reactions to the formation of CO can be found by integrating their reactions rates during the gas residence time, and comparing the resulting values with the total production rate of CO. That analysis showed that the most important reactions leading to CO_2 splitting are electron impact dissociation (E1) and dissociative electron attachment (E9), the contribution of these reactions being 97% and 2%, respectively. It was also found that dissociative recombination of positive ions CO_2^+ with electrons to form CO and O (R1) is not as important for CO_2 splitting as in DBD discharges [15].

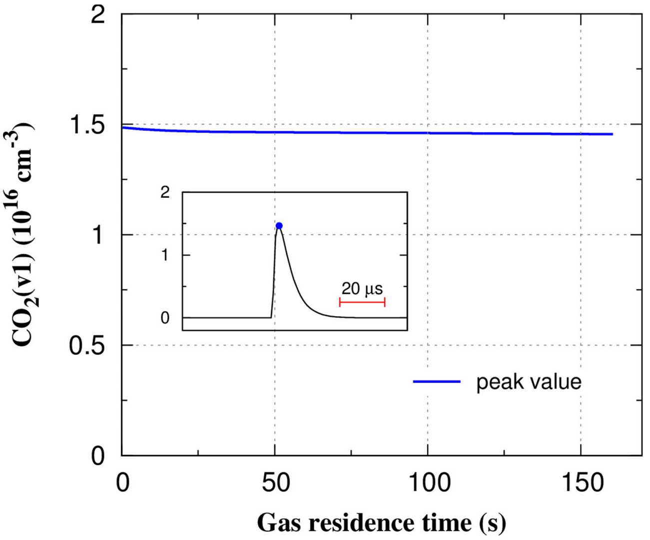

Figure 8. Peak values of the number density of CO_2(v1) as a function of the gas residence time, t_g (numerical simulation). The insets show the temporal evolution of a single peak occurring at $t_g \approx 100$ s.

Table 3. Relaxation times to half peak of vibrationally excited states of CO_2 generated in pulsed corona discharge in pure CO_2 (numerical modeling).

CO_2(v1)	CO_2(v2)	CO_2(v3)	CO_2(v4)
~6.0 μs	~2.0 μs	~2.0 μs	~2.0 μs

The number densities of the other ground state neutral species, C and C_2O, are much smaller (see figure 7). This is due to the low production rate of these species, which only takes place during the duration of pulses (reactions E11 and N6), and their fast conversion back into CO and CO_2 again, mostly through reactions N7, N10, N13, N15 and N16. As a result, the concentrations of C and C_2O exhibit rapid fluctuations over time, since they are only present during the development of pulses. The main plots in figure 7 show the temporal evolution of peak values of C and C_2O density, while the actual variation of the number density during the development of a single pulse is shown in the insets.

The number densities of all ions fall drastically to negligible values after each pulse. Although it is possible to include long living ions in the model, there is an important lack of information in the literature regarding their kinetics.

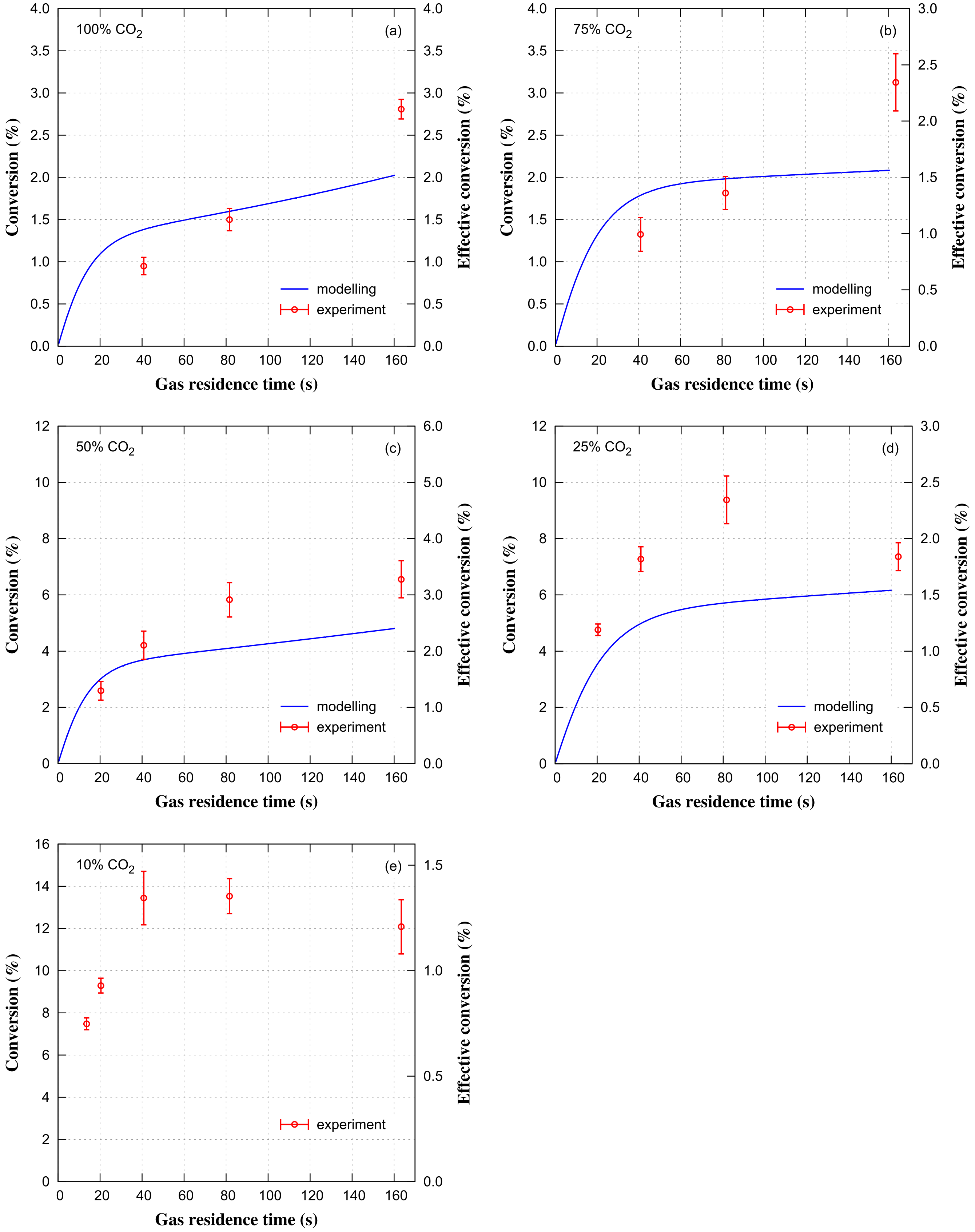

Figure 9. Carbon dioxide conversion to carbon monoxide as function of residence time for (a) pure CO_2, (b) 75% CO_2 and 25% Ar, (c) 50% CO_2 and 50% Ar, (d) 25% CO_2 and 75% Ar (e) 10% CO_2 and 90% Ar. Solid line: numerical simulation, dots: experimental measurements.

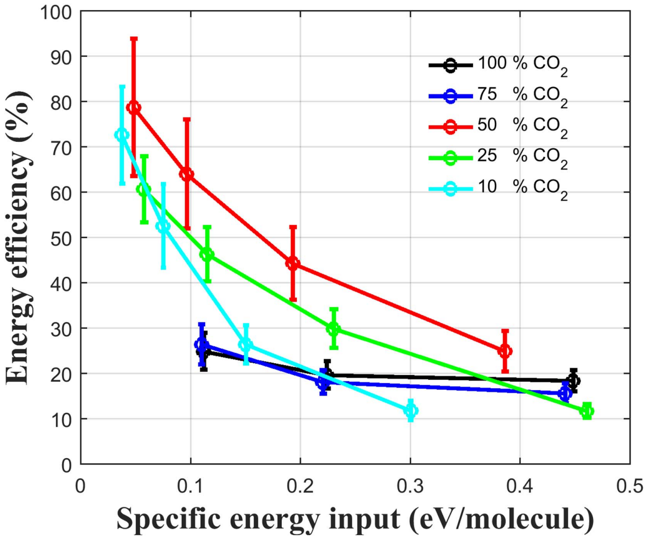

Figure 10. Experimental energy efficiency as function of the specific input energy for different gas mixtures of Ar and CO_2. 1 eV $molecule^{-1}$ ≈ 3.933 J cm^{-3} at 1 atm and 298 K.

Moreover, other works [34] that have included these long living charged species have noted that their contribution to CO_2 splitting is minimal. Therefore, these types of ions were excluded in our model for simplicity.

Regarding vibrationally excited molecules, figure 8 shows the number density of the lowest vibrationally excited level of CO_2(v1) as a function of gas residence time. Higher vibrationally excited states exhibit a similar temporal dependence, but the peak density values, which are reached at every pulse, are different: they are of the order of 1.5×10^{16} for CO_2(v1), 6×10^{15} for CO_2(v2), 6×10^{15} for CO2(v3) and 1.5×10^{15} for CO_2(v4). This sequence of values derives from the different energy thresholds of vibrational levels and the existence of vibration–vibration (VV) and vibration–translation (VT) exchange processes [2]. The highest density of vibrational states (CO_2(v1)) is about three orders of magnitude lower than the density of the ground state of CO_2. After each pulse, the population of vibrationally excited molecules initiates a rapid decay through the aforementioned relaxation of higher vibrational states to lower levels and to the ground state (table A5). The decay of vibrational species lasts from 2 to 6 μs (see table 3), which is much shorter than the period between pulses. Since during the inter pulse phase there is no further production of excited states, no accumulation occurs before the application of the next pulse. Therefore, although vibrational excitations have the largest reaction rates during the pulse and vibrationally excited CO_2 could undergo dissociation through reaction E10 (table A1), quenching reactions becomes dominant in the long term, owing to the large concentration of CO_2, CO and O_2. This is the primary reason why vibrational states do not contribute significantly to CO_2 dissociation in nanosecond pulsed corona discharge, according to the numerical simulation. However, the inclusion of vibrational states in the model is important, since they contribute to the electron energy gain/loss term in (3), and electron impact reactions depend ultimately on electron energy.

If the pulse repetition frequency was to be increased, so that the onset of subsequent pulses is before the period of relaxation, accumulation of the vibrational states would occur and this would result in a different pathway to CO_2 dissociation. It is predicted that the frequency required to increase the role of vibrational level of CO_2 is in excess of 100 kHz. Due to the limitations of the HV pulse generator used in this work it was not possible to test such high frequencies. Owing to complications from using fast rise time pulses, it may indeed not be possible to operate at high frequencies and voltages as electromagnetic interference becomes a concern from an experimental standpoint, although it could be numerically modeled.

3.2. Results for mixtures of Ar/CO_2

Figure 9 shows the CO_2 conversion, X_{conv}, produced by the nanosecond pulsed corona discharge versus the gas residence time t_g for different gas mixtures of Ar/CO_2. Again, an acceptable qualitative agreement between simulation and experiments was found for SEI up to 0.5 eV $molecule^{-1}$, which are reached for gas residence times of about 150 s. However, as the percentage of Ar in the feed increases the model becomes less accurate which is attributed to the change in behavior of the discharge which tends away from homogeneity.

Clearly, in all gas mixtures, there is an initial steep rise in CO_2 conversion as the residence time increases. Then, the growth rate slows down but keeps increasing in mixtures containing 50% CO_2 or less. However, for gas mixtures containing a higher concentration of argon, and at residence times above 80 s, the conversion of CO_2 plateaus and begins to decrease, i.e. increasing the residence time further has a detrimental effect. The lowest absolute conversions were found in the case of a pure CO_2 plasma (figure 9(a)), but they increased significantly upon addition of Ar. For example, in 90% Ar mixtures, the absolute conversion increases up to 15%. However, in such a mixture, the electrical discharge is not homogeneous, since there is a transition from glow to the spark regime. As a consequence, the predictions of the model, which assumes a homogeneous discharge, deviate from the experimental measurements.

The absolute energy efficiency of the CO_2 splitting process is shown in figure 10 as a function of the specific input energy for different gas mixtures of CO_2/Ar. The energy efficiency tends to decrease as the SEI is raised, which happens when the gas flow rate is reduced (long gas residence times).

Table 4 shows the absolute CO_2 conversions and efficiencies reported by other researchers using different plasma sources and gaseous mixtures. A direct comparison between different works is not straightforward, since the specific energy involved in each experiment may differ considerably. For example, Ramakers *et al* [17] and Snoeckx *et al* [21] have studied, respectively, the conversion of CO_2 in mixtures with

Table 4. Comparison of absolute CO_2 conversion and energy efficiencies reported in the literature using different plasma sources and gas mixtures.

		25% CO_2		50% CO_2		100% CO_2	
Plasma source	SEI (J cm^{-3})	X_{conv} (%)	η (%)	X_{conv} (%)	η (%)	X_{conv} (%)	η (%)
DBD in CO_2/Ar [17]	~8	13	19	8.4	13	5	9.2
DBD in CO_2/N_2 [21]	~12	12	13	7.7	8	3.3	3.3
Pulsed discharge in CO_2 (2.36 atm) [7]	~4.4	—	—	—	—	3.5	11.5
Pulsed corona in CO_2/Ar (this work)	~0.85	9.4	30	5.8	44	1.5	20

Ar and N_2 using DBD. According to their observations, the absolute conversion increased with the addition of the impurities. Moreover, in mixtures with CO_2 contents of 50% and 25%, the conversions achieved in CO_2/Ar were similar to that in CO_2/N_2. In the present work, the conversions found using pulsed corona in CO_2/Ar are slightly smaller, but they were obtained with SEI one order the magnitude lower than the ones used in the DBD. As a consequence, the energy efficiencies of CO_2 conversion using pulsed corona are substantially higher. The two last columns in table 4 correspond to the conversion and efficiencies found in pure CO_2. In addition to the experiments of Ramakers *et al* [17] and Snoeckx [21], the observations of Bak *et al* [7], corresponding to a nanosecond pulsed discharge, are also presented in the table. Again, the conversions achieved using DBD and nanosecond pulsed discharge were higher, but the corresponding energy efficiencies were substantially lower compared to the present experiments.

The high efficiency achieved in the CO_2/Ar pulsed corona discharge can be attributed to two concurring points: firstly, only a small fraction of the input energy goes towards excitation and ionization of Ar, and secondly, the introduction of Ar reduces the breakdown voltage of the gas mixture, which in turn increases the electron density.

To illustrate the first point, figure 11(a) shows the radial distribution of the mean electron energy and electric field for a single pulse at three different times, according to the numerical simulation. Clearly, the electron energy is closely correlated to the electric field, and the later is affected by the presence of the spatial charge. Alongside figure 11(a), the corresponding electron density is represented in figure 11(b). These distributions correspond to a mixture of 75% CO_2 and 25% Ar, but they are qualitatively similar in other mixtures of CO_2/Ar. As discussed in section 2.1, the voltage waveform was constituted of a first nanosecond sub-pulse of high amplitude (~17 kV) and a subsequent sequence of smaller sub-pulses, with amplitudes in the range of 1–3 kV. As shown in figure 11(a), the electron energy is very high during the occurrence of the main nanosecond sub-pulse ($t \approx 7 \times 10^{-8}$ s) and, therefore, most of the electrical energy supplied to the reactor goes towards ionization of Ar and CO_2 and excitation of lower and higher vibrational levels of CO_2. However, during the subsequent sub-pulses ($t > 7 \times 10^{-8}$ s), the electron energy is lower, and most of the energy will go towards excitation of lower vibrational states of CO_2 and direct electron impact dissociation of CO_2. This is so due to the high energy threshold required for electron impact excitation and ionization of Ar (11.55 eV and 15.76 eV, respectively). Conversely, the energy thresholds of inelastic collisions of electrons with CO_2 molecules are much lower: 6.23 eV for the lowest electronic excitation level, 5.52 eV for dissociation and only 0.08 eV for vibrational excitation to the lowest vibrational level. Since the energy deposited into the plasma during the development of these small amplitude sub-pulses represents, approximately, 93% of the whole electrical discharge energy, the processes occurring during this phase of the pulse has a great influence in the overall mechanism of CO_2 splitting.

What has been mentioned in the foregoing discussion would not certainly lead on its own to an increase of energy efficiency of CO_2 splitting in CO_2/Ar mixtures. However, as it has already been indicated, the addition of Ar also alters the breakdown potential of the gas mixture. As explained in [17], the Townsend ionization coefficient is one order of magnitude higher in Ar than in CO_2. Therefore, the addition of Ar gives rise to a substantial reduction of the breakdown voltage and, as a consequence, the number density of electrons is significantly increased. This effect can be clearly appreciated in figure 12, where the spatially averaged electron density has been plotted as a function of time for different CO_2/Ar mixtures. Compared to the case of pure CO_2, in a gas mixture with 50% of Ar the electron density has risen by 30% (at the peak of current) to 60% (at ~1 μs). Thus, during the first nanosecond sub-pulse, electron densities in excess of 10^{11} cm^{-3} are reached. Once this first sub-pulse is extinguished, the high population of electrons decays slowly over time and, according to the model, promotes the dissociation of CO_2 by electron impact during the subsequent sub-pulses of lower amplitude.

As shown in figure 13, the average electron temperature also rises upon increasing the argon percentage in the gas mixture. Therefore, the addition of Ar produces a substantial increase of the reaction rate constants of electron impact dissociation of CO_2, as shown in table 5. However, in contrast to the average electron density, the highest energies were found in the gas mixture with the highest Ar content (75% Ar). This is explained by the fact the ionization is not only related to the electron energy, but also to the electron energy distribution function.

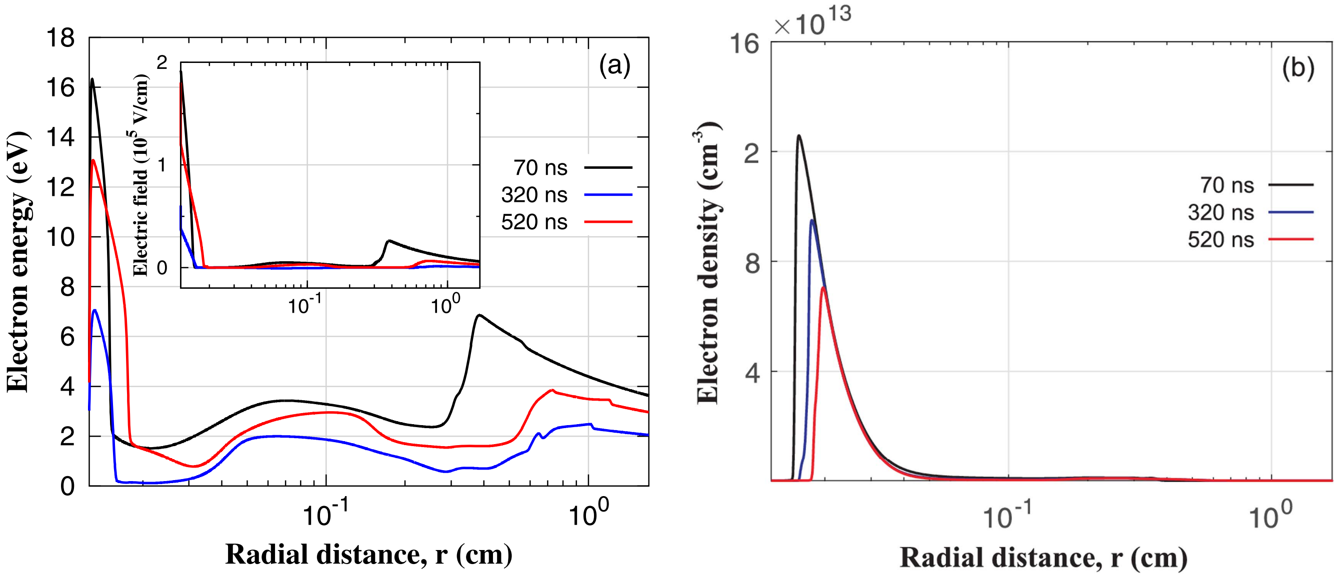

Figure 11. Spatial distribution of (a) electron energy and electric field (inset) and (b) electron density at different times during one pulse in a mixture of 75% CO_2 and 25% Ar, calculated from the 1D model.

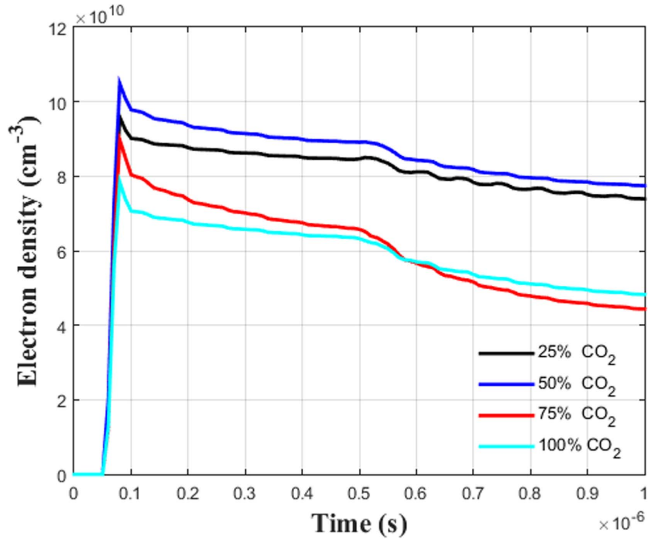

Figure 12. Temporal evolution of the spatially averaged electron density calculated from the 1D model during a pulse in different gas mixtures.

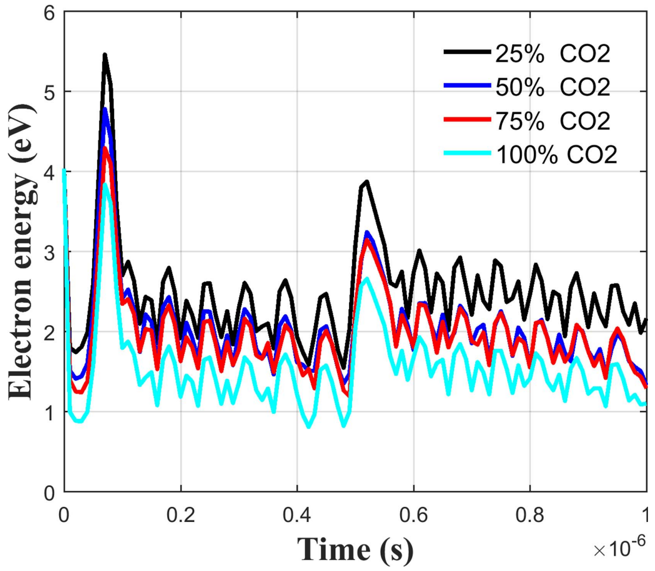

Figure 13. Spatially averaged electron energy calculated from the 1D model during a single pulse for different gas mixtures.

Table 5. Spatially averaged reactions rate constants of electron impact dissociation of CO_2 for different gas mixtures (1D model).

Gas mixture	Reaction rate constant (cm^{-3} s^{-1})
Pure CO_2	5.64×10^{-12}
75% CO_2 and 25% Ar	1.00×10^{-11}
50% CO_2 and 50% Ar	1.10×10^{-11}
25% CO_2 and 75% Ar	1.09×10^{-11}

Experimentally, the percentage of Ar that yields the best efficiency was found to be 50% (figure 10). This observation is in accordance with the averaged numerical results presented in figure 12 and in table 5, since the highest electron density and the largest electron impact dissociation rate constant of CO_2 were also found for that mixture. Moreover, very high percentages of Ar tend to produce plasma instabilities and transition towards a non-homogeneous spark discharge, which reduces the efficiencies of CO_2 splitting as energy is diverted away from electron impact dissociation of CO_2.

Finally, it is worth noting that, besides the beneficial effect to CO_2 splitting produced by the addition of Ar, the pathway leading to CO_2 dissociation in a nanosecond pulsed corona discharge appears different from other types of non-thermal discharges, according to the results of the numerical model built.

As reported by Fridman [2] and Aerts *et al* [19], the process of CO_2 splitting in electric discharges depends on whether the electron energy transfer to a CO_2 molecule is via excitation, ionization, or dissociation. For example, in a DBD discharge, the energy efficiency for CO_2 splitting is limited because the reduced electric field is high ($\sim$200 Td), which corresponds to a mean electron energy of about 4.5 eV [19]. This energy is too high to produce a significant population of CO_2 vibrational levels [35]. Therefore, in the region of operation of DBD discharges, most of the electron energy goes into electronic excitation, while the remaining energy is distributed among vibrational excitation, dissociation and ionization. Thus, vibrational excitation is of minor importance in a DBD discharge.

In contrast, the first vibrational level of the asymmetric stretching mode is known to provide the most important channel for the CO_2 splitting in microwave discharges [2, 16]. This is so because the typical values of the reduced electric field are around 20–40 Td, which corresponds to mean electron energies in the range 1.5–3 eV [19]. Therefore, most of electron energy is transferred to vibrational excitation of CO_2 molecules. However, although microwave discharges have very high energy efficiencies, they have the disadvantage of being usually operated at reduced pressure [35], which requires an additional energy input and, therefore, reduces the overall efficiency of CO_2 splitting.

According to the results obtained from the numerical modeling (figure 13), the averaged electron energy in our pulsed corona discharge changes over time from operating in the DBD energy region to the microwave energy region. However, although the population of lower vibrational levels becomes important during the discharge, they quickly relax back to the ground state on a scale of several microseconds, in the interval between two consecutive pulses. Therefore, its direct contribution to CO_2 splitting is of secondary importance, but they must be retained for a correct modeling of the pulsed corona discharge. As previously discussed, pulsed corona discharge should be operated at much higher frequencies in order to these vibrational states accumulate and play a more significant role to CO_2 splitting.

4. Conclusion

Nanosecond pulsed corona discharge in carbon dioxide and its mixtures with argon have been experimentally and numerically investigated.

A plasma-chemical model has been built to simulate the operation of a pulsed corona discharge reactor. In order to yield accurate results within a reasonable computational time-frame, the model has incorporated a selection of reactions and species of the complex CO_2/Ar plasma chemistry, and it has combined 1D and 0D models for the transport equations.

The model has been tested and validated under the conditions of a homogeneous discharge, and the results obtained showed an excellent qualitative agreement with the experimental measurements. However, it was observed during the experimental measurements that transition to spark occurred in CO_2/Ar mixtures rich in Ar ($>$75%). In such conditions, the model assumptions are violated and it can no longer give an accurate representation of the discharge.

The high voltage waveform produced by the nanosecond power supply (and incorporated to the simulation) has shown to have important implications on the kinetics of CO_2 splitting. It was constituted by a first nanosecond sub-pulse of high amplitude ($\sim$17 kV) followed by a series of smaller sub-pulses, with amplitudes in the range of 1–3 kV. Owing to this particular waveform, the process of CO_2 splitting proceeded along a two-step pathway. Firstly, during the high amplitude sub-pulse, the electron density and the electron energy increase rapidly, and inelastic collisions lead primarily to ionization and vibrational excitations of CO_2 and Ar. During the subsequent sub-pulses, electrons promote the dissociation of CO_2 by direct impact and the excitation of low vibrational levels of CO_2.

The best result in terms of absolute conversion ($\sim$14%) was achieved in a gas mixture of 10% CO_2–90% Ar. However, the best energy efficiency ($\sim$80%) was obtained when CO_2 and Ar were in the ratio 1:1. Compared to other plasma sources, like DBD, the energy efficiency of the conversion process was significantly higher. This can be attributed to the specific form of the applied voltage waveform and its short duration. In contrast to other traditional plasma sources, energy is delivered in high intensity bursts of nanosecond duration, thus avoiding the need for long residence times to achieve similar conversions.

Acknowledgments

This research has been funded by the EPSRC from the 4CU Programme Grant (EP/K001329/1), at the University of Sheffield. F Pontiga also acknowledges the support of the Spanish Government Agency 'Ministerio de Economía y Competitividad' under contract no. FIS2014-54539-P. The authors also wish to thank Dr T Butterworth and Dr D Kuvshivov for numerous discussions and help with the experimental setup.

Appendix. List of chemical reactions

Reaction rate constants are expressed in $cm^3\,s^{-1}$ for two-body reactions, and in $cm^6\,s^{-1}$ for three-body reactions.

Cross section data were extracted from the database indicated in the cited reference and reaction rate constants were calculated using Bolsig+ [40, 41].

Table A1. Electron impact reactions.

Number	Reaction	Rate constant	Reference
(E1)	$\mathbf{e^- + CO_2 \rightarrow e^- + CO + O}$	$f(\sigma)$	[39]
(E2)	$\mathbf{e^- + CO_2 \rightarrow e^- + CO_2(v1)}$	$f(\sigma)$	[36]
(E3)	$\mathbf{e^- + CO_2 \rightarrow e^- + CO_2(v2)}$	$f(\sigma)$	[36]
(E4)	$\mathbf{e^- + CO_2 \rightarrow e^- + CO_2(v3)}$	$f(\sigma)$	[36]
(E5)	$\mathbf{e^- + CO_2 \rightarrow e^- + CO_2(v4)}$	$f(\sigma)$	[36]
(E6)	$\mathbf{e^- + CO_2 \rightarrow e^- + CO_2{}^*}$	$f(\sigma)$	[36]
(E7)	$\mathbf{e^- + CO_2 \rightarrow 2e^- + CO_2^+}$	$f(\sigma)$	[36]
(E8)	$e^- + CO_2 \rightarrow 2e^- + CO + O^+$	$f(\sigma)$	[36]
(E9)	$\mathbf{e^- + CO_2 \rightarrow CO + O^-}$	$f(\sigma)$	[33]
(E10)	$\mathbf{e^- + CO_2(vx) \rightarrow e + CO + O}$	$f(\sigma)$	[36]
(E11)	$e^- + CO \rightarrow e^- + C + O$	1.0×10^{-12}	[37]
(E12)	$e^- + O_2 \rightarrow e^- + O + O$	4.0×10^{-9}	[15]
(E13)	$e^- + O_2 \rightarrow 2e^- + O_2^+$	1.8×10^{-11}	[38]
(E14)	$e^- + O_3 \rightarrow O + O_2^-$	8.9×10^{-12}	[38]
(E15)	$e^- + O_3 \rightarrow O_2 + O^-$	2.0×10^{-10}	[38]
(E16)	$\mathbf{e^- + Ar \rightarrow e^- + Ar^*}$	$f(\sigma)$	[33]
(E17)	$\mathbf{e^- + Ar \rightarrow 2e^- + Ar^+}$	$f(\sigma)$	[33]
(E18)	$\mathbf{e^- + Ar^* \rightarrow 2e^- + Ar^+}$	$f(\sigma)$	[33]
(E19)	$\mathbf{e^- + CO_2 \rightarrow e^- + CO_2}$	$f(\sigma)$	[33]
(E20)	$\mathbf{e^- + Ar \rightarrow e^- + Ar}$	$f(\sigma)$	[33]

Table A2. Electron–ion recombination reactions.

Number	Reaction	Rate constant	Reference
(R1)	$e^- + CO_2^+ \rightarrow CO + O$	6.5×10^{-7}	[15]
(R2)	$e^- + Ar^+ + Ar \rightarrow Ar + Ar$	1.0×10^{-25}	Est. from [28]

Table A3. Neutral–neutral reactions.

Number	Reaction	Rate constant	Reference
(N1)	$O + O_2 + M \rightarrow O_3 + M$	5.85×10^{-34} (M = O_2) 1.81×10^{-33} (M = CO_2)	[9]
(N2)	$O + O + M \rightarrow O_2 + M$	1.04×10^{-32} (M = CO_2)	[9]
(N3)	$O + O_3 \rightarrow O_2 + O_2$	8.5×10^{-15}	[9]
(N4)	$O_3 + M \rightarrow O_2 + O + M$	4.0×10^{-15} (M = O_2)	[9]
(N5)	$O + CO + M \rightarrow CO_2 + M$	1.1×10^{-35} (M = CO_2)	[9]
(N6)	$C + CO + M \rightarrow C_2O + M$	6.3×10^{-32} (M = CO_2)	[9]
(N7)	$O + C_2O \rightarrow CO + CO$	5.0×10^{-11}	[9]
(N8)	$CO_2 + CO_2 \rightarrow CO + O + CO_2$	$3.91 \times 10^{-10} \exp(-49\,430/T_g)$	[20, 37]
(N9)	$CO_2 + O \rightarrow CO + O_2$	$2.8 \times 10^{-11} \exp(-26\,500/T_g)$	[20, 37]
(N10)	$CO_2 + C \rightarrow CO + CO$	1.0×10^{-15}	[20, 37]
(N11)	$O_2 + CO \rightarrow CO_2 + O$	$4.2 \times 10^{-12} \exp(-24\,000/T_g)$	[7, 20]
(N12)	$O_3 + CO \rightarrow CO_2 + O_2$	4.0×10^{-25}	[20, 37]
(N13)	$O_2 + C \rightarrow CO + O$	3.0×10^{-11}	[20]
(N14)	$O_3 + M \rightarrow O_2 + O + M$	$4.12 \times 10^{-10} \exp(-11\,430/T_g)$ (M = Ar)	[20, 37]
(N15)	$O_2 + C_2O \rightarrow CO_2 + CO$	3.3×10^{-13}	[20]
(N16)	$O + C + M \rightarrow CO + M$	$2.14 \times 10^{-29}(T_g/300)^{-3.08} \exp(-2114/T_g)$ (M = CO_2)	[20, 37]

Table A4. Ion–ion and ion–molecule reactions.

Number	Reaction	Rate constant	Reference
(I1)	$O^- + CO_2 + M \rightarrow CO_3^- + M$	9×10^{-29} $(M = CO_2)$	[9]
(I2)	$O_2^- + CO_2 + M \rightarrow CO_4^- + M$	1.0×10^{-29} $(M = CO_2)$	[9, 20, 37]
(I3)	$O_2^- + CO_2^+ \rightarrow CO + O_2 + O$	6.5×10^{-7}	[20]
(I4)	$O^+ + CO_2 \rightarrow O_2^+ + CO$	9.4×10^{-10}	[20]
(I5)	$O^+ + CO_2 \rightarrow CO_2^+ + O$	4.5×10^{-10}	[20, 37]
(I6)	$CO_2^+ + O \rightarrow O^+ + CO_2$	9.62×10^{-11}	[20]
(I7)	$CO_2^+ + O_2 \rightarrow O_2^+ + CO_2$	5.3×10^{-11}	[20]
(I8)	$CO_3^- + CO_2^+ \rightarrow CO_2 + CO_2 + O$	5.0×10^{-7}	[20]
(I9)	$O_2^+ + CO_3^- \rightarrow CO_2 + O_2 + O$	3.0×10^{-7}	[20, 37]
(I10)	$O_2^+ + CO_4^- \rightarrow CO_2 + O_2 + O_2$	3.0×10^{-7}	[20, 37]
(I11)	$CO_3^- + O \rightarrow O_2^- + CO_2$	8.0×10^{-11}	[20]
(I12)	$CO_4^- + O \rightarrow CO_3^- + O_2$	1.1×10^{-10}	[20]
(I13)	$CO_4^- + O \rightarrow O^- + CO_2 + O_2$	1.4×10^{-11}	[20]
(I14)	$O^+ + O_2 \rightarrow O_2^+ + O$	$1.9 \times 10^{-11} (T_g/300)^{-0.5}$	[20, 37]
(I15)	$O_2^- + O^+ + M \rightarrow O_3 + M$	2.0×10^{-25} $(M = CO_2)$	[20]
(I16)	$O_2^- + O^+ \rightarrow O + O_2$	2.7×10^{-7}	[20]
(I17)	$O_2^- + O_2^+ \rightarrow O_2 + O_2$	2.0×10^{-7}	[20]
(I18)	$O_2^- + O_2^+ \rightarrow O + O + O_2$	4.2×10^{-7}	[20]
(I19)	$O_2^- + O_2^+ + M \rightarrow O_2 + O_2 + M$	2.0×10^{-25} $(M = O_2)$	[20]
(I20)	$O^- + O^+ \rightarrow O + O$	4.0×10^{-8}	[20]
(I21)	$O^- + O^+ + M \rightarrow O_2 + M$	2.0×10^{-25} $(M = O_2)$	[20]
(I22)	$O^- + O_2^+ \rightarrow O_2 + O$	1.0×10^{-7}	[20]
(I23)	$O^- + O_2^+ \rightarrow O + O + O$	2.6×10^{-8}	[20]
(I24)	$O^- + O_2^+ + M \rightarrow O_3 + M$	2.0×10^{-25} $(M = O_2)$	[20]

Table A5. Average reaction rate coefficients for vibrational relaxation to the ground state (V–T relaxation) and vibrational relaxation between two different energy levels (V–V relaxation).

Number	Reaction	Rate constant	Reference
(V1)	$CO_2(v1) + CO_2 \rightarrow CO_2 + CO_2$	1.07×10^{-14}	[19]
(V2)	$CO_2(v1) + CO \rightarrow CO_2 + CO$	7.48×10^{-15}	[19]
(V3)	$CO_2(v1) + O_2 \rightarrow CO_2 + O_2$	7.48×10^{-15}	[19]
(V4)	$CO_2(v2) + CO_2 \rightarrow CO_2 + CO_2$	9.00×10^{-16}	[19]
(V5)	$CO_2(v2) + CO \rightarrow CO_2 + CO$	2.79×10^{-17}	[19]
(V6)	$CO_2(v2) + O_2 \rightarrow CO_2 + O_2$	2.79×10^{-17}	[19]
(V7)	$CO_2(v2) + CO_2 \rightarrow CO_2(v1) + CO_2$	2.90×10^{-14}	[19]
(V8)	$CO_2(v2) + CO \rightarrow CO_2(v1) + CO$	2.03×10^{-14}	[19]
(V9)	$CO_2(v2) + O_2 \rightarrow CO_2(v1) + O_2$	2.03×10^{-14}	[19]
(V10)	$CO_2(v3) + CO_2 \rightarrow CO_2(v2) + CO_2$	7.72×10^{-16}	[19]
(V11)	$CO_2(v3) + CO \rightarrow CO_2(v2) + CO$	2.32×10^{-16}	[19]
(V12)	$CO_2(v3) + O_2 \rightarrow CO_2(v2) + O_2$	3.09×10^{-16}	[19]
(V13)	$CO_2(v3) + CO_2 \rightarrow CO_2(v4) + CO_2$	6.05×10^{-15}	[19]
(V14)	$CO_2(v3) + CO \rightarrow CO_2(v4) + CO$	1.81×10^{-15}	[19]
(V15)	$CO_2(v3) + O_2 \rightarrow CO_2(v4) + O_2$	2.42×10^{-15}	[19]
(V16)	$CO_2(v3) + CO_2 \rightarrow CO_2(v1) + CO_2(v2)$	2.42×10^{-15}	[19]
(V17)	$CO_2(v2) + CO \rightarrow CO_2(v1) + CO$	1.70×10^{-18}	[19]
(V18)	$CO_2(v2) + O_2 \rightarrow CO_2(v1) + O_2$	5.10×10^{-19}	[19]
(V19)	$CO_2(v3) + O_2 \rightarrow CO_2(v1) + O_2$	6.80×10^{-19}	[19]
(V20)	$CO_2(v4) + CO_2 \rightarrow CO_2(v2) + CO_2$	4.33×10^{-14}	[19]
(V21)	$CO_2(v4) + CO \rightarrow CO_2(v2) + CO$	3.03×10^{-14}	[19]
(V22)	$CO_2(v4) + O_2 \rightarrow CO_2(v2) + O_2$	3.03×10^{-14}	[19]
(V23)	$CO_2(v4) + CO_2 \rightarrow CO_2(v1) + CO_2$	9.08×10^{-18}	[19]
(V24)	$CO_2(v4) + CO \rightarrow CO_2(v1) + CO$	6.18×10^{-15}	[19]
(V25)	$CO_2(v4) + O_2 \rightarrow CO_2(v1) + O_2$	6.18×10^{-15}	[19]

References

[1] United Nations Framework Convention on Climate Change, Conference of the Parties (COP) 2015 *Adoption of the Paris Agreement, Proposal by the President (Geneva, Switzerland)* FCCC/CP/2015/L.9/Rev.1

[2] Fridman A 2008 *Plasma Chemistry* (Cambridge: Cambridge University Press)

[3] Yamamoto T, Ramanathan K, Lawless P A, Ensor D S, Newsome J R, Plaks N and Ramsey G H 1992 Control of volatile organic compounds by an ac energized ferroelectric pellet reactor and a pulsed corona reactor *IEEE Trans. Ind. Appl.* **28** 528–34

[4] Helfritch D J 1993 Pulsed corona discharge for hydrogen sulfide decomposition *Non-Thermal Plasma Techniques for Pollution Control* (Berlin: Springer) pp 211–21

[5] Dinelli G, Civitano L and Rea M 1990 Industrial experiments on pulse corona simultaneous removal of NO_x and SO_2 from flue gas *IEEE Trans. Ind. Appl.* **26** 535–41

[6] Malik M A and Jiang X Z 1999 The CO_2 reforming of natural gas in a pulsed corona discharge reactor *Plasma Chem. Plasma Process.* **19** 505–12

[7] Bak M S, Im S K and Cappelli M 2015 Nanosecond-pulsed discharge plasma splitting of carbon dioxide *IEEE Trans. Plasma Sci.* **43** 1002–7

[8] Xu W, Li M-W, Xu G-H and Tian Y-L 2004 Decomposition of CO_2 using DC corona discharge at atmospheric pressure *Japan. J. Appl. Phys.* **43** 8310–1

[9] Mikoviny T, Kocan M, Matejcik S, Mason N and Skalny J D 2004 Experimental study of negative corona discharge in pure carbon dioxide and its mixtures with oxygen *J. Phys. D: Appl. Phys.* **37** 64–73

[10] Horvath G, Skalný J D and Mason N J 2008 FTIR study of decomposition of carbon dioxide in dc corona discharges *J. Phys. D: Appl. Phys.* **41** 225207

[11] Pontiga F, Yanallah K, Moreno H, Hadji K and Castellanos A 2011 Negative corona discharge in mixtures of CO_2 and N_2: modeling and experiments *20th Int. Symp. on Plasma Chemistry (Philadelphia, USA, 24–29 July 2011*

[12] Pontiga F, Moreno H, Hadji K, Yanallah K and Castellanos A 2012 Experimental study of positive corona discharge in mixtures of CO_2 and N_2 *XXI Europhysics Conf. on the Atomic and Molecular Physics of Ionized Gases (Viana do Castelo, Portugal, 10–14 July 2012)*

[13] Hokazono H, Obara M, Midorikawa K and Tashiro H 1991 Theoretical operational life study of the closedcycle transversely excited atmospheric CO_2 laser *J. Appl. Phys.* **69** 6850–68

[14] Cenian A, Chernukho A, Borodin V and Śliwiński G 1995 Modeling of plasma-chemical reactions in gas mixture of CO_2 lasers: II. Theoretical model and its verification *Contrib. Plasma Phys.* **35** 273–96

[15] Aerts R, Somers W and Bogaerts A 2015 Carbon dioxide splitting in a dielectric barrier discharge plasma: a combined experimental and computational study *ChemSusChem.* **8** 702–16

[16] Bogaerts A, Kozak T, Laer K and Snoeckx R 2015 Plasma-based conversion of CO_2: current status and future challenges *Faraday Discuss.* **183** 217–32

[17] Ramakers M, Michielsen I, Aerts R, Meynen V and Bogaerts A 2015 Effect of argon or helium on the CO_2 conversion in a dielectric barrier discharge *Plasma Processes Polym.* **12** 755–63

[18] Snoeckx R, Aerts R, Tu X and Bogaerts A 2013 Plasma-based dry reforming: a computational study ranging from the nanoseconds to seconds time scale *J. Phys. Chem.* C **117** 4957–70

[19] Aerts R, Martens T and Bogaerts A 2012 Influence of vibrational states on CO_2 splitting by dielectric barrier discharges *J. Phys. Chem.* C **116** 23257–73

[20] Kosak T and Bogaerts A 2014 Splitting of CO_2 by vibrational excitation in non-equilibrium plasmas: a reactions kinetics model *Plasma Sources Sci. Technol.* **23** 045004

[21] Snoeckx R, Heijkers S, Van Wesenbeeck K, Lenaerts S and Bogaerts A 2016 CO_2 conversion in a dielectric barrier discharge plasma: N_2 in the mix as a helping hand or problematic impurity? *Energy Environ. Sci.* **9** 999–1011

[22] Yanallah K, Pontiga F, Meslem Y and Castellanos A 2012 An analytical approach to wire-to-cylinder corona discharge *J. Electrostat.* **70** 374–83

[23] Yanallah K, Pontiga F, Moreno H and Castellanos A 2010 Physico-chemical modeling of positive corona discharge in carbon dioxide *2010 Annual Report Conf. on Electrical Insulation and Dielectric Phenomena (West Lafayette, Indiana, USA, 17–20 October 2010)* pp 397–400

[24] Lyublinsky A G, Korotkov S V, Aristov Y V and Korotkov D A 2013 Pulse power nanosecond-range DSRD-based generators for electric discharge technologies *IEEE Trans. Plasma Sci.* **41** 2625–9

[25] Yousfi M, Poinsignon A and Hamani A 1994 Finite element method for conservation equations in electrical gas discharge areas *J. Comput. Phys.* **113** 268–78

[26] Soria C, Pontiga F and Castellanos A 2004 Plasma chemical and electrical modelling of a negative dc corona in pure oxygen *Plasma Sources Sci. Technol.* **13** 95–107

[27] Boeuf J P 1987 Numerical model of RF glow discharges *Phys. Rev.* A **36** 2782–92

[28] *COMSOL Multiphysics* v. 5.2. (www.comsol.com), COMSOL AB, Stockholm, Sweden

[29] Pancheshnyi S, Eismann B, Hagelaar G J M and Pitchford L C 2008 *Computer code ZDPlasKin* University of Toulouse, LAPLACE, CNRS-UPS-INP, Toulouse, France (http://zdplaskin.laplace.univ-tlse.fr)

[30] Pai D Z, Lacoste D A and Laux C O 2010 Transitions between corona, glow, and spark regimes of nanosecond repetitively pulsed discharges in air at atmospheric pressure *J. Appl. Phys.* **107** 093303

[31] Akishev Y, Grushin M, Kochetov I, Karal'Nik V, Napartovich A and Trushkin N 2005 Negative corona, glow and spark discharges in ambient air and transitions between them *Plasma Sources Sci. Technol.* **14** S18–25

[32] Kulikovsky A A 1995 A more accurate Scharfetter-Gummel algorithm of electron transport for semiconductor and gas discharge simulation *J. Comput. Phys.* **119** 149–55

[33] Morgan W L and Penetrante B M 1990 ELENDIF: a time-dependent Boltzmann solver for partially ionized plasmas *Comput. Phys. Commun.* **58** 127–52

[34] Aerts R 2014 Experimental and computational study of dielectric barrier discharges for environmental applications *PhD Thesis* Universiteit Antwerpen

[35] Kozak T and Bogaerts A 2015 Evaluation of the energy efficiency of CO_2 conversion in microwave discharges using a reaction kinetics model *Plasma Sources Sci. Technol.* **24** 015024

[36] Hayashi M 1990 Electron collision cross sections determined from beam and swarm data by Boltzmann analysis *Nonequilibrium Processes in Partially Ionized Gases* ed M Capitelli and J N Bardsley (New York: Plenum) Hayashi Database (www.lxcat.net), retrieved on 15 June 2016

[37] Beuthe T G and Chang J S 1997 Chemical kinetic modelling of non-equilibrium Ar–CO_2 thermal plasmas *Japan. J. Appl. Phys.* **36** 4997–5002

[38] Eliasson B and Kogelschatz U 1986 Basic data for modelling of electrical discharges in gases: oxygen *Technical Report* KLR 86-11 C ABB Asea Brown Boveri

[39] Corvin K K and Corrigan S J 1969 Dissociation of carbon dioxide in the positive column of a glow discharge *J. Chem. Phys.* **50** 2570–4

[40] Hagelaar G J M BOLSIG+: Electron Boltzman equation Solver, http://bolsig.laplace.univ-tlse.fr (Accessed: July 2015)

[41] Hagelaar G J M and Pitchford L C 2005 Solving the Boltzmann equation to obtain electron transport coefficients and rate coefficients for fluid models *Plasma Sources Sci. Technol.* **14** 722–33